Classification: Biological Sciences: Cell biology

Title: A cancer-associated polymorphism in ESCRT-III disrupts the abscission checkpoint and promotes genome instability

Authors: Jessica B.A. Sadler[1†], Dawn M. Wenzel[2†], Lauren K. Williams[2,7], Marta Guindo-Martínez[3], Steven L. Alam[2], Josep Maria Mercader[3,4,5], David Torrents[3,6], Katharine S. Ullman[7], Wesley I. Sundquist[2]* and Juan Martin-Serrano[1]*

Affiliations:

[1] Department of Infectious Diseases, King's College London, Faculty of Life Sciences & Medicine, London SE1 9RT, UK.

[2] Department of Biochemistry, University of Utah School of Medicine, Salt Lake City, UT 84112-5650, USA.

[3] Barcelona Supercomputing Center (BSC). Joint BSC-CRG-IRB Research Program in Computational Biology, 08034 Barcelona, Spain.

[4] Programs in Metabolism and Medical & Population Genetics, Broad Institute of Harvard and MIT, Cambridge, Massachusetts, USA.

[5] Diabetes Unit and Center for Genomic Medicine, Massachusetts General Hospital, Boston, Massachusetts, USA.

[6] Institució Catalana de Recerca i Estudis Avançats (ICREA).

[7] Department of Oncological Sciences, Huntsman Cancer Institute, University of Utah, Salt Lake City, UT 84112, USA.

* Correspondence to: wes@biochem.utah.edu, juan.martin_serrano@kcl.ac.uk.

[†] These authors contributed equally to this work

Keywords: Abscission, Cytokinesis, ESCRT, CHMP4C, Checkpoint

Abstract

Cytokinetic abscission facilitates the irreversible separation of daughter cells. This process requires the Endosomal Sorting Complexes Required for Transport (ESCRT) machinery and is tightly regulated by Charged Multivesicular body Protein 4C (CHMP4C), an ESCRT-III subunit that engages the abscission checkpoint (NoCut) in response to mitotic problems such as persisting chromatin bridges within the midbody. Importantly, a human polymorphism in $CHMP4C^{T232}$ (rs35094336), increases cancer susceptibility. Here, we explain the structural and functional basis for this cancer association: the $CHMP4C^{T232}$ allele unwinds the C-terminal helix of CHMP4C, impairs binding to the early-acting ESCRT factor ALIX, and disrupts the abscission checkpoint. Cells expressing $CHMP4C^{T232}$ exhibit increased levels of DNA damage and are sensitized to several conditions that increase chromosome mis-segregation, including DNA replication stress, inhibition of the mitotic checkpoint, and loss of p53. Our data demonstrate the biological importance of the abscission checkpoint, and suggest that dysregulation of abscission by $CHMP4C^{T232}$ may synergize with oncogene-induced mitotic stress to promote genomic instability and tumorigenesis.

Significance Statement

The final step of cell division, abscission, is temporally regulated by the Aurora B kinase and CHMP4C in a conserved pathway called the abscission checkpoint which arrests abscission in the presence of lingering mitotic problems. Despite extensive study, the physiological importance of this pathway to human health has remained elusive. We now demonstrate that a cancer predisposing polymorphism in CHMP4C disrupts the abscission checkpoint and results in DNA damage accumulation. Moreover, deficits in this checkpoint synergize with p53 loss and generate aneuploidy under stress conditions that increase the frequency of chromosome missegregation. Therefore, cells expressing the cancer-associated polymorphism in CHMP4C are genetically unstable, thus suggesting a novel oncogenic mechanism that may involve the dysregulation of abscission.

Manuscript body

Introduction

Cytokinetic abscission is the final stage of cell division when the newly formed daughter cells are irreversibly separated. Abscission is a multi-step process that culminates in the resolution of the midbody, the thin intercellular bridge that connects dividing cells following mitosis (1-3). The final membrane fission step of abscission is mediated by the Endosomal Sorting Complexes Required for Transport (ESCRT) pathway (4-7). The ESCRT machinery comprises membrane-specific adaptors and five core factors/complexes (ALIX,

37   ESCRT-I, ESCRT-II, ESCRT-III and VPS4), which are recruited sequentially (8-10). During

38   cytokinesis, the midbody adaptor protein CEP55 initially recruits the early-acting ESCRT

39   factors ALIX and ESCRT-I (4, 5, 11, 12). These factors, in turn, promote the recruitment and

40   polymerization of essential ESCRT-III subunits such as CHMP4B, to form filaments within the

41   midbody. These membrane-associated filaments collaborate with the AAA ATPase VPS4 to

42   constrict and sever the midbody (4-6, 11, 13).

43   Abscission is tightly coordinated with earlier stages of mitosis to ensure faithful

44   inheritance of genetic material during cell division (14). In particular, cytokinetic abscission is

45   temporally regulated by a conserved mechanism known as the abscission checkpoint (NoCut

46   in yeast), which delays abscission in response to mitotic problems such as incomplete

47   nuclear pore reformation or chromatin bridges within the midbody (15-19). The abscission

48   checkpoint is governed by the master regulator, Aurora B kinase, which inhibits ESCRT-III

49   activity in response to mitotic problems. Two key intersecting signaling nodes within this

50   pathway are the ESCRT-III subunit CHMP4C and the regulatory ULK3 kinase. CHMP4C is a

51   specialized ESCRT-III subunit that is dispensable for cytokinetic membrane fission, viral

52   budding and endosomal sorting, but plays an essential role in executing the abscission

53   checkpoint (20, 21). CHMP4C is directly phosphorylated by Aurora B and is further

54   phosphorylated by ULK3, which also phosphorylates other ESCRT-III subunits such as IST1.

55   CHMP4C phosphorylation and ULK3 activity, together with the actions of other ESCRT-III-

56   associated factors such as ANCHR, collectively prevent ESCRT-III polymerization and

57   sequester VPS4 away from abscission sites, thereby delaying abscission (20, 22, 23).

58   Despite recent advances in identifying key components of the abscission checkpoint,

59   the biological functions of the checkpoint and its contributions to human health are not yet

60   known. Here, we have addressed these questions by analyzing the biochemical and

61   abscission checkpoint activities of rs35094336, a human *CHMP4C* polymorphism (minor

62   allele frequency [MAF]=0.04) associated with increased susceptibility to ovarian cancer (24).

63   rs35094336 encodes an amino acid substitution of A232 (CHMP4C^{A232}; reference allele) to

64   T232 (CHMP4C^{T232}; risk allele). Here, we show that the A232T substitution induces structural

65   changes that impair ALIX binding and that cells expressing the CHMP4C^{T232} risk allele lack

66   an abscission checkpoint and accumulate genetic damage. The CHMP4C^{T232} allele also

67   sensitizes cells to chromosome mis-segregation and induces aneuploidy when the spindle

68   assembly checkpoint is weakened. These observations demonstrate the importance of the

69   abscission checkpoint in maintaining genetic stability and suggest a novel oncogenic

70   mechanism in which disruption of the abscission checkpoint by CHMP4C^{T232} may contribute

71   to tumorigenesis by synergizing with oncogenic mutations that increase mitotic stress.

3

Results

CHMP4C^{T232} is associated with multiple cancer types

The CHMP4C^{T232} allele was initially identified in a meta-analysis of two genome wide association studies (GWAS) of single nucleotide polymorphisms associated with ovarian cancer (24). To test for an association of the CHMP4C^{T232} polymorphism with other cancers, we mined data from 337,208 individuals in the UK Biobank search engine (25). Our analysis of this independent cohort confirmed the previously identified association with ovarian cancer, and revealed statistically significant associations with multiple other types of cancer, including male genital tract, prostate, and skin (Table 1). Although the odds ratios for these associations are relatively modest (1.04-1.17), association of the variant with increased risk for multiple different cancers suggests that this allele could be involved in a general pathway toward genetic instability and tumorigenesis.

CHMP4C^{T232} exhibits reduced ALIX binding

Position 232 is the penultimate CHMP4C residue, and A232 lies within a C-terminal helix that forms the ALIX binding site (26). We therefore tested whether the A232T amino acid substitution affected ALIX binding, and found that this substitution significantly reduced the interaction between full length CHMP4C and ALIX (but not CHMP4C and itself) in a yeast two-hybrid assay (Fig. 1A). This substitution similarly inhibited the ability of a GST-fused C-terminal CHMP4C peptide (residues 216-233) to pull down endogenous ALIX from HeLa cell lysates (Fig. S1A) and reduced the affinity of the terminal CHMP4C peptide for the pure recombinant ALIX Bro1 domain (residues 1-359) by 13-fold as measured in a competitive fluorescence polarization binding assay (Fig. 1B). In each case, we observed complete loss of ALIX binding to well-characterized control CHMP4C mutants that lacked key hydrophobic contact residues (L228A and/or W231A)(26).

To determine the molecular basis for this reduction in ALIX binding affinity, we determined high-resolution crystal structures of terminal CHMP4C^{A232} and CHMP4C^{T232} peptides (residues 216-233) bound to the ALIX Bro1 domain (residues 1-359) (Fig. 1C and Fig. S1B, C and Table S1) (26). Comparison of the structures revealed that although both peptides bound the same surface groove of the Bro1 domain, the A232T substitution disrupted several key ALIX interactions (Fig. 1D). Specifically, the A232T substitution unwound the C-terminal end of the terminal CHMP4C helix (Fig. 1C, and Fig. S1D), altered the position of CHMP4C residue W231, and disrupted intermolecular hydrogen bonds between the W231 carbonyl oxygen and indole nitrogen with ALIX residues D143 and K147, respectively (Fig. 1D). These structural analyses suggested that the A232T substitution might induce CHMP4C helix unwinding by introducing a beta-branched amino acid (which reduces

4

108 helical propensity) and/or by prematurely capping the CHMP4C C-terminal helix (27). Indeed,

109 both of these effects appeared to be operative because mutant CHMP4C peptides that

110 selectively retained only beta-branching (CHMP4C^{A232V}) or capping potential (CHMP4C^{A232S})

111 exhibited intermediate (3-4-fold) reductions in ALIX peptide binding affinity (Fig. 1*B*).

112 Together, these analyses demonstrate that the CHMP4C^{T232} risk allele alters the structure of

113 the CHMP4C C-terminal helix, removes key ALIX interactions, and reduces ALIX binding

114 affinity by more than an order of magnitude.

115

116 **ALIX-CHMP4C interactions are required for abscission checkpoint activity**

117 ALIX is a key initiator of the cytokinetic abscission cascade (4, 5, 11, 28), and

118 CHMP4C plays an essential role in maintaining the abscission checkpoint (4, 20, 21). We

119 therefore tested whether abscission checkpoint activity was affected by CHMP4C mutations

120 that impaired ALIX binding, including the CHMP4C^{T232} risk allele. In these experiments,

121 siRNA treatment was used to deplete endogenous CHMP4C from HeLa cells engineered to

122 stably express different siRNA-resistant HA-CHMP4C proteins (Fig. 2, and Fig. S2). Partial

123 depletion of nuclear pore components Nup153 and Nup50 was used to activate the

124 abscission checkpoint. As expected, control cells that expressed endogenous CHMP4C

125 stalled during abscission, as indicated by elevated midbody connections, whereas cells

126 depleted of CHMP4C did not exhibit elevated levels of midbody connections (20, 29) (Fig.

127 2A, Fig. S2*A*). Importantly, checkpoint activity was rescued in cells that expressed HA-

128 CHMP4C^{A232} but not in cells that expressed HA-CHMP4C^{T232}, implying that the CHMP4C^{T232}

129 risk allele does not support the abscission checkpoint. The HA-CHMP4C^{L228A,W231A} mutant

130 also failed to support the abscission checkpoint, further indicating that the CHMP4C-ALIX

131 interaction is required to sustain the checkpoint. Notably, the loss of checkpoint activity for

132 both HA-CHMP4C^{L228A,W231A} and HA-CHMP4C^{T232} was comparable to the defective response

133 observed in cells that expressed an inactive control CHMP4C mutant lacking the amino acid

134 insertion phosphorylated by Aurora B (HA-CHMP4C^{-INS})(20, 21). Similarly, cells expressing

135 only HA-CHMP4C^{T232}, HA-CHMP4C^{L228A,W231A} or HA-CHMP4C^{-INS} also proceeded through

136 abscission more rapidly under normal growth conditions, implying that they were insensitive

137 to steady-state abscission checkpoint activity, likely induced by midbody tension (23, 30)

138 (Fig. 2*B*, Fig. S2*B*, Movies S1-S6). Despite these defects, HA-CHMP4C^{A232}, HA-

139 CHMP4C^{T232}, HA-CHMP4C$^{L228A, W231A}$ and HA-CHMP4C^{-INS} were all recruited to the midbody

140 at normal levels, whether or not nucleoporins were depleted (Fig. 2*D, E*). Additionally,

141 CHMP4C ALIX-binding mutants and wildtype CHMP4C proteins were mitotically

142 phosphorylated at comparable levels (Fig. S2*D*), indicating that the CHMP4C mutations did

143 not disrupt recognition by Aurora B or ULK3 kinases, and that ALIX binding is not required for

144 these activities. These observations imply that abscission checkpoint activity requires ALIX

145 binding to CHMP4C. We find, however, that CHMP4C midbody localization does not require

146 ALIX binding, in contrast to a previous report (28).

147 To test CHMP4C^{T232} activity when the abscission checkpoint was activated by a

148 different trigger, we used live cell imaging to measure the resolution times of intercellular

149 chromatin bridges, as visualized using the nuclear envelope marker lamina-associated

150 polypeptide 2β fused to YFP (YFP-LAP2β). As expected (20), chromatin bridges were

151 resolved prematurely in CHMP4C-depleted cells compared to cells that expressed

152 endogenous CHMP4C^{A232} (median resolution time = 250 vs 685 min, Fig. 2*C*, Fig. S2*C*,

153 Movies S7-S12). Importantly, normal midbody resolution times were restored by expression

154 of siRNA-resistant HA-CHMP4C^{A232} (800 min), but not by HA-CHMP4C^{T232} (200 min), HA-

155 CHMP4C^{L228A,W231A} (300 min) or HA-CHMP4C^{-INS} (340 min). Thus, cells expressing the

156 cancer-associated CHMP4C^{T232} risk allele lack an appropriate abscission checkpoint

157 response under multiple different conditions that activate this checkpoint.

158

159 **Disruption of the abscission checkpoint leads to accumulation of DNA damage**

160 Although the biological consequences of abscission checkpoint loss are not well

161 understood, increased DNA damage is one possible outcome (20). We therefore compared

162 DNA damage accumulation in cells that expressed the different CHMP4C mutants. In these

163 experiments, CRISPR-Cas9 was used to delete the CHMP4C locus from HCT116 cells (Fig.

164 S3), a near diploid cell line that exhibits low levels of chromosomal instability and DNA

165 damage (31). Genetic damage was then assessed by scoring the number of nuclear foci

166 formed by the DNA damage response marker 53BP1. As expected, cells with low levels of

167 DNA damage predominated in the wild type cultures (HCT116^{WT}) (<2 foci/cell) (Fig. 3*A*, *B*). In

168 contrast, cells lacking CHMP4C (HCT116^{δCHMP4C}) exhibited heightened DNA damage (>6

169 foci/cell) with significantly greater frequency. Crucially, DNA damage in the HCT116^{δCHMP4C}

170 cells was reduced to control levels upon re-expression of HA-CHMP4C^{A232}, but not HA-

171 CHMP4C^{T232}, HA-CHMP4C^{L228A,W231A} or HA-CHMP4C^{-INS}. Hence, loss of the CHMP4C-

172 dependent abscission checkpoint increases the accumulation of 53BP1-associated DNA

173 damage foci.

174

175 **CHMP4C is not required for maintenance of nuclear integrity, DNA damage responses**

176 **nor mitotic checkpoint signaling.**

177 To determine whether observed phenotypes were specifically due to abscission

178 checkpoint failure, we examined other mechanisms that might underlie the elevated levels of

179 DNA damage in HCT116^{δCHMP4C} cells. We ruled out ESCRT-dependent loss of nuclear

6

180 envelope integrity (32, 33) because nuclear envelope compartmentalization was not
181 compromised during telophase in cells lacking CHMP4C, as assayed by nuclear morphology
182 and retention of a GFP-NLS reporter (Fig. S4 and Movies S13-S15). Similarly, loss of
183 CHMP4C did not globally impair DNA damage responses because the efficiency of G2/M cell
184 cycle arrest in response to genotoxic stress induced by the DNA cross-linker mitomycin C
185 was normal in HCT116$^{\delta CHMP4C}$ cells (Fig. S5). Furthermore, in contrast to another report (34),
186 we did not observe a failure of HCT116$^{\delta CHMP4C}$ cells to arrest in response to spindle poisons
187 such as nocodazole, indicating that the spindle assembly checkpoint remains largely intact in
188 these cells (Fig. S6). Therefore, the increased DNA damage in cells lacking CHMP4C activity
189 and a functional abscission checkpoint does not reflect loss of nuclear integrity, improper
190 DNA damage responses or defective mitotic spindle assembly checkpoint signaling but
191 rather a loss of the abscission checkpoint.

192

193 **CHMP4C^{T232} sensitizes cells to replication stress**

194   We next examined the possibility that cells lacking CHMP4C activities had increased
195 levels of DNA damage because they were unable to respond properly to DNA replication
196 stress. This is an attractive model because: 1) a significant fraction of 53BP1 nuclear bodies
197 originate from lesions generated by DNA replication stress (35), 2) elevated replication stress
198 triggers the abscission checkpoint in a CHMP4C-dependent manner (18) (Fig. 3*C*), and 3)
199 the abscission checkpoint plays a key role in protecting anaphase bridges that arise from
200 replication stress (36), thereby reducing damage when they persist during cytokinetic
201 abscission (37). In agreement with this model, inducing replication stress with ultra-low doses
202 (30 nM) of the DNA polymerase inhibitor aphidicolin reduced the proliferation of
203 HCT116$^{\delta CHMP4C}$ cells nearly 2-fold as compared to HCT116^{WT} cells (Fig. 3*D*). Importantly, the
204 HCT116$^{\delta CHMP4C}$ growth defect was again rescued by expression of HA-CHMP4C^{A232}, but not
205 by the abscission checkpoint defective, HA-CHMP4C^{T232}, HA-CHMP4C^{L228A,W231A} or HA-
206 CHMP4C^{-INS} mutants. Thus, the abscission checkpoint can play a protective role in cell
207 survival when cells are subjected to increased replication stress.

208

209 **CHMP4C^{T232} sensitizes cells to chromosome mis-segregation and induces aneuploidy**

210   To examine the functions of the abscission checkpoint in the context of another mitotic
211 stress, we tested whether a defective abscission checkpoint also sensitized cells to
212 weakening of the spindle assembly checkpoint (SAC), a condition that induces anaphase
213 chromosomal segregation errors. The SAC was selectively weakened by treatment with low
214 doses (0.1 µM) of the MPS1 kinase inhibitor reversine (38), which doubled the frequency of
215 anaphase chromosome mis-segregation (Fig. 4*A*, Fig. S7*B*, Movies S16-19) and activated

216 the abscission checkpoint in a CHMP4C-dependent fashion (Fig. S7A). Karyotyping of
217 metaphase spreads revealed that HCT116^{WT} cells only rarely displayed extreme aneuploidy
218 (1% of DMSO-treated cells had <37 or >48 chromosomes, Fig. 4B, C). Reversine treatment
219 alone increased this percentage, but cells with extreme aneuploidy were still rare (7%). In
220 contrast, DMSO treated HCT116$^{\delta CHMP4C}$ cells exhibited a higher basal level of extreme
221 aneuploidy (4%), and this percentage increased notably upon reversine treatment (23%). Re-
222 expression of HA-CHMP4C^{A232}, but not HA-CHMP4C^{T232} protected against reversine induced
223 increases in aneuploidy (Fig. S8A). Importantly, reversine treatment in cells with a defective
224 abscission checkpoint did not induce a multinucleation phenotype, but these cells did display
225 a higher proportion of micronuclei (Figure S8B).

226   In a complementary set of experiments, we monitored cell growth rates in reversine-
227 treated cultures, where the high levels of chromosomal instability and aneuploidy are
228 detrimental to cell survival and growth (39) (Fig. 4E, top panel). In agreement with the
229 karyotype analyses, reversine treatment reduced HCT116^{WT} cell growth only modestly, but
230 reduced HCT116$^{\delta CHMP4C}$ cell growth by at least 70% over a seven-day period. Robust growth
231 in the presence of reversine was restored by expression of HA-CHMP4C^{A232}, but not HA-
232 CHMP4C^{T232}, HA-CHMP4C^{L228A,W231A} or HA-CHMP4C^{-INS} (Fig. 4E, top panel). Thus, the
233 CHMP4C-dependent abscission checkpoint becomes more critical for cell growth under
234 conditions that increase chromosome segregation defects.

235

236 **CHMP4C^{T232} synergizes with p53 loss**

237   Our observations that CHMP4C mutations can abolish the abscission checkpoint and
238 that these mutations synergize with increases in chromosome mis-segregation raised the
239 intriguing possibility that such mutations might also synergize with genetic alterations known
240 to be associated with ovarian cancer development. We focused our studies on TP53, the
241 most frequently mutated gene in a wide range of cancers, including >96% of high-grade
242 serous ovarian tumors (40). In addition to its classical role in inducing cell cycle arrest in
243 response to DNA damage, p53 also functions directly in DNA damage repair and
244 chromosomal stability, and its absence is associated with increased replicative stress (41).
245 As expected, stable depletion of p53 increased DNA damage levels as measured by
246 increased numbers of 53BP1 foci (Fig. S9B, C) and increased frequencies of chromosomal
247 segregation defects during anaphase (Fig. 4D, S7D, Movies S20-S23). As with reversine
248 treatment, these defects significantly compromised HCT116 cell growth only when CHMP4C
249 was absent (Fig. 4E, bottom panel, Fig. S9A). This synergistic effect was again reversed
250 upon re-expression of CHMP4C^{A232} but not HA-CHMP4C^{T232}, HA-CHMP4C^{L228A,W231A} or HA-
251 CHMP4C^{-INS} (Fig. 4E, bottom panel, Fig. S9A). Thus, loss of the CHMP4C-dependent

252   abscission checkpoint also synergizes with loss of functional p53. This effect can again be

253   explained by an inability of cells to cope with the increased burden of chromosomal

254   segregation defects, perhaps compounded further by dysfunction of the p53-mediated G1

255   checkpoint (42).

256

257   **Discussion**

258   Our study demonstrates that the abscission checkpoint plays a critical role in human

259   health by protecting the genome against DNA damage and chromosomal instability. We have

260   shown that a human polymorphism in *CHMP4C,* previously associated with increased

261   susceptibility to ovarian cancer, is also associated with increased risk for several other

262   cancers, thus suggesting that the CHMP4C^{T232} allele contributes to tumor development in a

263   global fashion. Importantly, cells that express the cancer-associated CHMP4C^{T232} allele show

264   elevated levels of 53BP1 foci, suggesting that increased DNA damage may account, at least

265   in part, for increased cancer susceptibility in individuals who carry this allele. Furthermore,

266   cells that express CHMP4C^{T232} are particularly sensitized to genomic instability under

267   conditions that increase the burden of chromosomal segregation defects, such as DNA

268   replication stress and weakening of the spindle assembly checkpoint.

269   At the mechanistic level, the A232T substitution unwinds the C-terminal CHMP4C

270   helix, impairs ALIX binding affinity, and leads to loss of abscission checkpoint activity. Hence,

271   in addition to the previously documented requirements for CHMP4C phosphorylation by

272   Aurora B and ULK3 (20, 21, 23), CHMP4C must also be able to interact with ALIX (and

273   possibly other Bro-domain containing proteins) to support the abscission checkpoint. We

274   found, however, that altered CHMP4C midbody localization could not explain the loss of

275   checkpoint activity because point mutations that specifically abolished ALIX binding did not

276   reduce CHMP4C midbody localization or mitotic phosphorylation. In contrast, others have

277   observed reduced midbody localization of a C-terminally truncated CHMP4C construct (28).

278   It is therefore possible that the C-terminal region of CHMP4C dictates midbody localization

279   independently of ALIX binding, perhaps through interactions with MKLP1 or the

280   Chromosomal Passenger Complex (20, 43). Alternatively, removal of 18 terminal CHMP4C

281   residues could have relieved CHMP4C autoinhibition, thereby impairing midbody localization

282   indirectly. This idea is consistent with the observation that autoinihibition of Snf7p, the yeast

283   orthologue of CHMP4, can be relieved by removing its terminal Bro1p (ALIX) binding helix

284   (44-46). We do not yet know for certain why CHMP4C-ALIX binding is required to support the

285   abscission checkpoint, but one intriguing possibility is that CHMP4C binding may

286   competitively inhibit CHMP4B from occupying its overlapping binding site on ALIX (26),

9

287 thereby sustaining the abscission checkpoint by preventing nucleation of CHMP4B-
288 containing ESCRT-III filaments within the midbody.

289   Another striking finding of our study is that increasing chromosomal segregation
290 defects in cells lacking a functional abscission checkpoint specifically induces high levels of
291 aneuploidy and chromosomal instability. Although complete inhibition of Aurora B leads to
292 cleavage furrow regression and binucleation when chromatin is present in the intracellular
293 bridge (17), this mechanism does not appear to explain the increases in aneuploidy when
294 CHMP4C is impaired. Depletion of CHMP4C (or other abscission checkpoint components
295 downstream of Aurora B such as ULK3) induces premature resolution of chromatin bridges,
296 not furrow regression (20, 23). Moreover, reversine treatment in cells lacking CHMP4C does
297 not lead to multinuleation, but does induce micronuclei formation. Our data are consistent
298 with chromosomal instability resulting from chromosome breakage and refusion events,
299 and/or the failure to re-incorporate lagging chromosomes into the main nuclei. It has been
300 suggested that even very mild aneuploidy has consequences beyond chromosome gains or
301 losses, resulting in DNA damage and replication stress which have severe effects on
302 subsequent mitoses, and that even gain of a single chromosome can result in further
303 chromosomal aberrations and complex karyotypes in subsequent cell cycles (47, 48). We
304 suggest that DNA damage acquired over a number of cell cycles in cells lacking a functional
305 abscission checkpoint may have cumulative effects that are ultimately detrimental in
306 subsequent cell cycles. Consistent with this idea, damage acquired during mitosis can lead to
307 p53-dependent quiescence in daughter cells (47, 48). Thus, the coordinated action of the
308 abscission checkpoint and p53 may protect against aneuploidy. In this model, the abscission
309 checkpoint provides additional time to retrieve, repair and/or protect lagging chromosomes,
310 thereby protecting cells and preventing catastrophic DNA damage during mitosis. Disruption
311 of the abscission checkpoint could also induce aneuploidy via a mechanism that is
312 reminiscent of the checkpoint adaptation phenomenon, in which cells continue to proceed
313 through the cell cycle despite not having completely resolved DNA damage arising the
314 previous mitosis (51). Such checkpoint-adapted cells are characterized by severe
315 chromosomal segregation defects that give rise to micronuclei containing lagging
316 chromosomes (or chromosome fragments), which then contribute to further chromosome
317 damage and instability in subsequent divisions.

318   Chromosomal segregation errors are a hallmark of many cancers and often arise in
319 response to oncogenic mutations that increase mitotic stress (39). In particular, loss of p53 is
320 the most common genetic abnormality in many tumor types, and can lead to increased DNA
321 damage, chromosomal instability, and increased replicative stress (40, 41, 50). These
322 phenotypes suggest a potential mechanism by which loss of the abscission checkpoint could

10

323   contribute to genetic instability and cancer development, particularly as we observed
324   synthetic lethality between loss of p53 and the CHMP4C^{T232} risk allele. Our data suggest the
325   possibility that homozygous germline expression of the CHMP4C^{T232} allele - or loss of
326   heterozygosity of CHMP4C^{A232} encoding allele expression in somatic cells where the T232
327   encoding allele is present - could contribute to tumorigenesis by increasing genomic
328   instability and aneuploidy, particularly when chromosome mis-segregation events are
329   elevated.   We speculate that although an impaired abscission checkpoint combined with
330   genetic alterations such as p53 loss is detrimental to overall cell growth, the subset of cells
331   that ultimately survive may accumulate further adaptations that promote tumorigenicity.
332   These cells may nevertheless remain sensitive to further perturbations of chromosome
333   segregation or DNA damaging agents and this sensitivity could, in principle, be exploited
334   therapeutically. In this regard, it is noteworthy that CHMP4C depletion increases the
335   effectiveness of irradiation-induced apoptosis in human lung cancer cells (51) and that many
336   common chemotherapeutic drugs such as Paclitaxel act, at least in part, by increasing
337   chromosome mis-segregation (39). Hence, we speculate that such chemotherapeutics may
338   be particularly effective in patients who carry the CHMP4C^{T232} allele.

11

339   **Methods**

340

341   **Plasmids and antibodies:**

342   Details of plasmids and antibodies used in this study are described in Table S2.

343

344   **Fluorescence polarization (FP) binding experiments:**

345   Fluorescence polarization was measured using a Biotek Synergy Neo Multi-Mode plate

346   reader (Biotek) with excitation at 485 nm and detection at 528 nm. For competitive binding

347   experiments, the wild type CHMP4C peptide (residues 216-233) was synthesized with a non-

348   native cysteine at the N-terminus (CQRAEEEDDDIKQLAAWAT), and labeled with Oregon

349   Green 488 (Life Technologies/Molecular Probes 06,034) following manufacturer's

350   instructions. The labeled peptide was quantitated by the absorbance of Oregon Green 488 at

351   491 nm (extinction coefficient 83,000 cm^{-1} M^{-1} in 50 mM potassium phosphate, pH 9).

352   Different concentrations (as determined by absorbance at 280 nm) of unlabeled, N-terminally

353   acetylated CHMP4C peptides were titrated against a CHMP4C^{A232}-ALIX Bro1-V complex

354   created by mixing 5 μM ALIX Bro1-V and 0.5 nM fluorescently labeled CHMP4C^{A232} peptide

355   in binding buffer (20 mM sodium phosphate pH 7.2, 150 mM NaCl, 5 mM BME, 0.01%

356   Tween-20, and 0.2 mg/mL Bovine Serum Albumin). IC(50)s were calculated from binding

357   curves using Kaleidagraph (Synergy Software) and converted to K(i) (54). Competitive

358   binding curves were measured independently ≥7 times for each peptide and mean±SD K(i)

359   values are reported. All peptides were synthesized by the University of Utah Peptide

360   Synthesis Core Facility, and verified by mass spectrometry.

361

362   **GST Pull-Downs**:

363   GST-fused CHMP4C peptides spanning the ALIX binding helix (residues 216-233) from

364   CHMP4C^{A232} or the CHMP4C^{L228A,W231A} or CHMP4C^{T232} mutants were purified, immobilized

365   on glutathione-Sepharose agarose beads, and incubated with clarified HeLa cell lysates.

366   Bound material was analysed by SDS-PAGE followed by immunoblotting or Coomassie

367   staining. A detailed description is provided by SI Materials and Methods.

368

369   **Cell culture:**

370   HEK293T, HeLa and HCT116 cells were cultured and maintained in DMEM medium

371   supplemented with 10% fetal bovine serum and 20 μg/mL gentamycin. To generate stable

372   cell lines, 293T cells were transfected with retroviral packaging vectors (Table S2), MLV-

373   GagPol/pHIV 8.1 and pHIT VSVg at a ratio of 3:2:1 for 48 hours. 293T supernatant was

374   filtered through a 0.2 μm filter and used to transduce the indicated cell lines, with antibiotic

375 selection carried out 48 hours later. MycoAlert (Lonza) was used to screen for mycoplasma

376 contamination. HCT116 CRISPR cell lines were generated by transfection with retroviral

377 Cas9 expression plasmids containing specific guide RNAs targeting CHMP4C, and full

378 details are available in SI Materials and Methods.

379

380 **siRNA transfections:**

381 Cells were transfected with siRNA for 72 hours using Dharmafect 1 (Dharmacon) or

382 Lipofectamine RNAiMax (Thermofisher) according to manufacturers' instructions. Cells

383 received two transfections, once at 0 hours and again at 48 hours. For HeLa cells, CHMP4C

384 and non-targeting siRNA were used at 100 nM and Nup50 and Nup153 siRNA were used at

385 10 nM. For HCT116 cells, all siRNA was used at 10 nM. Cells were fixed or imaged 24 hours

386 after the second siRNA transfection. For GFP-NLS nuclear fluorescence recovery

387 experiments HCT116 cells were imaged 8 hours after the second transfection. siRNA

388 sequences used in this study have been described (16-19) and are available in Table S2.

389

390 **Immunoblotting:**

391 Cell lysates were denatured in Laemmli buffer, resolved by SDS–PAGE, and transferred to

392 Nitrocellulose membranes. Membranes were blocked with 5% skim milk in 0.1% Tween

393 20/TBS and incubated with primary antibodies in either 1% or 5% skim milk in blocking

394 solution for 3 hours at room temperature or overnight at 4°C. Membranes were washed in

395 0.1% Tween 20/TBS and incubated with the corresponding secondary antibodies conjugated

396 with HRP or near-Infrared fluorescent dyes in blocking solution for 1 hour at room

397 temperature and washed again. Proteins were detected and quantified using a Li-Cor

398 Odyssey Infrared scanner and software (Li-Cor Biosciences) or Image Quant LAS 400 (GE

399 Healthcare). Details on antibodies and dilutions can be found in Table S2.

400

401 **Immunofluorescence**:

402 Cells were grown on coverslips, washed once in PBS and fixed for 10-20 minutes in ice cold

403 methanol. Cells were blocked with 3% FCS, 0.1% Triton X-100 in PBS for 20 minutes.

404 Primary antibodies were applied for at least 1 hour. After washing 4X with PBS, secondary

405 antibodies were applied for 1 hour and nuclei were stained with either Hoechst or 4′,6-

406 diamidino-2-phenylindole (DAPI). Coverslips were mounted with ProLong Gold Antifade

407 Reagent (Invitrogen) on a microscope slide. Images were acquired using a Leica SP8

408 Confocal (Fig. 2*D*) or Nikon Ti-Eclipse wide-field inverted microscope (Fig. 3, S4, S2).

409 Scoring was conducted blind. Where indicated, deconvolution was performed using

410 HyVolution Pro-Automatic deconvolution software. Quantification of fluorescence staining

13

411   intensity was carried out with ImageJ. The freehand selection tool was used to outline the

412   region of interest and staining intensity within this area was measured. Signals were

413   background corrected using measurements from adjacent regions. Details on antibodies and

414   dilutions can be found in Table S2.

415

416   **Live cell imaging**:

417   Cells were seeded on glass-bottomed 24-well plates (MatTek) and transfected with siRNA or

418   shRNA or subjected to the specified drug treatments. Imaging was carried out for 24-72

419   hours on a Nikon Ti-Eclipse wide-field inverted microscope (Nikon 40 × 0.75 N.A. dry

420   objective lens) equipped with Perfect Focus system and housed in a 37℃ chamber (Solent

421   Scientific, UK) fed with 5% CO_2. Multiple fields of view were selected at various XY

422   coordinates, 3 Z slices were captured at a 1.25 μm spacing for HeLa cells and 1.8 μm

423   spacing for HCT116 cells. Images were acquired using a Hamamatsu Orca Flash 4.0 camera

424   (Hamamatsu Photonics, Japan), controlled by NIS-Elements software. For abscission time

425   measurements, images were acquired every 10 minutes for 48 hours and abscission time

426   was measured as the time from midbody formation to disappearance. For resolution timing

427   for YFP-Lap2β positive bridges, images were acquired every 20 minutes for 72 hours, and

428   resolution time was measured for time of appearance to disappearance of YFP-Lap2β

429   positive intercellular bridges. For nuclear accumulation of GFP–NLS and analysis of

430   anaphase defects, images were acquired every 5 minutes for 24 hours. Nuclear GFP signal

431   was identified through co-localization with H2B-mCherry, and was normalized to the

432   cytoplasmic signal. Signals were background corrected using measurements from adjacent

433   regions. Measurements were taken 10 frames before and 50 frames after nuclear envelope

434   breakdown, with cells depleted of CHMP7 serving as a positive control (56).

435

436   **Protein expression and purification:**

437   The human ALIX Bro1 domain (residues 1-359, Fig. 1*C, D*, Fig S1) and ALIX Bro1-V

438   domains (residues 1-698, Fig. 1*B*) were expressed and purified as previously described with

439   minor modifications (27, 57). A detailed description is provided by SI Materials and Methods.

440   Plasmids for bacterial expression of ALIX proteins are available from the Addgene plasmid

441   repository (www.addgene.org; see Table S2 for accession numbers).

442

443   **Crystallization and data collection:**

444   ALIX Bro1 crystallized in complex with CHMP4^{A232} or CHMP4C^{T232} peptides (residues 216-

445   233; N-terminally acetylated) at 20°C from sitting drops that contained 1.2 μL of protein (200

446   μM ALIX Bro1 and 220 μM CHMP4C peptide) and 0.7 μL of reservoir solution (CHMP4C^{A232}:

447   10% PEG 20,000, 100 mM MES, pH 6.5; CHMP4C^{T232}: 15% PEG 8,000, 100 mM MES, pH

448   6.5, 200 mM sodium acetate). Crystals were flash frozen in nylon loops in cryo-protectant

449   composed of reservoir solutions containing 30% glycerol. Data were collected remotely (58)

450   (0.9794 Å wavelength, 100°K) at the Stanford Synchrotron Radiation Lightsource (SSRL) on

451   beamline 12-2 using a Dectris Pilatus 6M detector. Data were integrated and scaled using

452   AutoXDS (59-61). Both complexes crystallized in space group C121 with one ALIX-

453   Bro1:CHMP4C complex in the asymmetric unit. The crystals diffracted to 1.91 Å (ALIX Bro1-

454   CHMP4C^{A232}) and 1.87 Å (ALIX Bro1-CHMP4C^{T232}) resolution. For data collection and

455   refinement statistics see Table S1.

456

457   **Structure determination and refinement:**

458   A model for molecular replacement was generated from the previously determined structure

459   of the ALIX Bro1-CHMP4C^{A232} complex (PDB 3C3R) (26) by removing the coordinates for the

460   CHMP4C peptide and using the ALIX Bro1 structure as a search model (Phaser in PHENIX)

461   (62, 63). CHMP4C helices were built *de novo* into the electron density for both structures

462   using Coot (64), and further refined in Phenix (65, 66) using TLS refinement strategies (67).

463   Final models had no outliers in the Ramachandran plot. Comparison of CHMP4C backbone

464   atoms from both structures reveal that the N-termini (residues 221-229) superimpose with a

465   0.223 Å RMSD, whereas the C-termini (residues 229-233) superimpose with a 1.14 Å RMSD.

466   Structures were analyzed and compared using PyMol (The PyMOL Molecular Graphics

467   System, Version 1.3). Structure coordinates have been deposited in the RCSB Protein

468   Databank with accession codes 5V3R and 5WA1 (ALIX Bro1-CHMP4C^{A232} and ALIX Bro1-

469   CHMP4C^{T232}, respectively).

470

471   **Cell growth assays:**

472   For assays examining the effect of low dose aphidicolin and reversine on cell growth cells

473   were seeded at a density of 2.5 x 10^4 cells per well of a 24 well plate in duplicate and a 12

474   well pate, treated 8 hours later with DMSO, 0.1 μM reversine or 30 nM aphidicolin, and left

475   undisturbed for 2,4, (in 24 well plate) or 7 days (in 12 well plate), except for a media refresh

476   after 4 days. Cell number was determined by manual counting at the indicated time points.

477   For analysis of cell growth following p53 depletion, cells were transduced with either control

478   or p53 shRNA for 48 hours, then antibiotic selected for a further 48 hours. Transduced cells

479   were seeded at a density of 2.5 x 10^4 cells in a single well of a 24 well plate, cell number was

480   determined at 2, 4, or 7 days. Cell number was determined by manual counting and cells

481   were re-seeded in to 12 well plates on day 2, or 6 well plates on day 4.

482

Karyotyping:

HCT116^{WT} or HCT116$^{\delta CHMP4C}$ cells were cultured for 48 hours in the presence of DMSO or 0.1 μM reversine and arrested in metaphase by overnight treatment with 50 ng/ml nocodazole. Cells were harvested, washed, treated in hypotonic buffer (10% FCS in ddH$_2$O) for 30 minutes at 37°C and fixed in methanol:acetic acid (3:1 ratio). Fixation solution was replaced 4 times and spreads were produced by dropping 16 μL solution onto a glass slide from a height of 10 cm in a humid environment. Chromosomes from >90 metaphase-arrested cells were counted.

Mitotic arrest assays:

To examine the role of CHMP4C in mitotic spindle function HCT116^{WT} or HCT116$^{\delta CHMP4C}$ cells were treated with 50ng/mL nocodazole, all cells were collected and analyzed by flow cytometry and western blotting. To examine the mitotic phosphorylation of CHMP4C, HeLa cells stably expressing indicated HA-CHMP4C constructs were treated with 2mM thymidine for 24 hours, washed, and treated with 50ng/mL Nocodazole overnight. All cells were collected and phosphorylation of HA-CHMP4C was determined by western blotting.

Flow cytometry analysis:

Cells treated overnight with 200 ng/mL mitomycin C, 50 ng/mL nocodazole or DMSO were harvested, washed in PBS and fixed in 1% paraformaldehyde. Cells were again washed and incubated with 50 µg/mL propidium iodide, 100 µg/mL RNase in PBS, and 0.1% Triton X-100. Cell cycle analysis profiles were acquired using FACS Canto II (BD Biosciences). 20,000 cells were counted per condition, and data were analyzed using FlowJo (Tree Start, Inc.). All gating was applied manually. For mitotic arrest experiments all conditions were performed in duplicate and samples were retained for immunoblotting analysis.

Analysis of publicly available cancer genome-wide association studies in the UK Biobank:

To determine if the CHMP4C rs35094336 variant is also associated with other cancer types we analyzed the publicly available data from 337,208 individuals in the UKBiobank engine. Results were obtained from Global Biobank Engine, Stanford, CA (URL: http://gbe.stanford.edu/) [October, 2017]. We used the following procedure to define cases and controls for cancer GWAS. Individual level ICD-10 codes from the UK Cancer Register, Data-Field 40006, and the National Health Service, Data-Field 41202 in the UK Biobank were mapped to the self-reported cancer codes, Data-Field 20001 as described previously (68).

16

518 Positive associations are displayed in Table 1. A full review of the resource is available in
519 reference (25).

520

521 **Acknowledgements:**

548 <div align="center">References</div>
549

550 1. Caballe A & Martin-Serrano J (2011) ESCRT machinery and cytokinesis: the road to
551   daughter cell separation. *Traffic* 12(10):1318-1326.

552 2. Fremont S, Romet-Lemonne G, Houdusse A, & Echard A (2017) Emerging roles of
553   MICAL family proteins - from actin oxidation to membrane trafficking during
554   cytokinesis. *J. Cell Sci.* 130(9):1509-1517.

555 3. Mierzwa B & Gerlich DW (2014) Cytokinetic abscission: molecular mechanisms and
556   temporal control. *Dev. Cell* 31(5):525-538.

557 4. Carlton JG & Martin-Serrano J (2007) Parallels between cytokinesis and retroviral
558   budding: a role for the ESCRT machinery. *Science* 316(5833):1908-1912.

559 5. Morita E*, et al.* (2007) Human ESCRT and ALIX proteins interact with proteins of the
560   midbody and function in cytokinesis. *EMBO J.* 26(19):4215-4227.

561 6. Guizetti J*, et al.* (2011) Cortical constriction during abscission involves helices of
562   ESCRT-III-dependent filaments. *Science* 331(6024):1616-1620.

563 7. Elia N, Sougrat R, Spurlin TA, Hurley JH, & Lippincott-Schwartz J (2011) Dynamics of
564   endosomal sorting complex required for transport (ESCRT) machinery during
565   cytokinesis and its role in abscission. *Proceedings of the National Academy of
566   Sciences of the United States of America* 108(12):4846-4851.

567 8. Schoneberg J, Lee IH, Iwasa JH, & Hurley JH (2017) Reverse-topology membrane
568   scission by the ESCRT proteins. *Nat. Rev. Mol. Cell Biol.* 18(1):5-17.

569 9. Christ L, Raiborg C, Wenzel EM, Campsteijn C, & Stenmark H (2017) Cellular
570   Functions and Molecular Mechanisms of the ESCRT Membrane-Scission Machinery.
571   *Trends Biochem. Sci.* 42(1):42-56.

572 10. Scourfield EJ & Martin-Serrano J (2017) Growing functions of the ESCRT machinery
573   in cell biology and viral replication. *Biochem Soc Trans* 45(3):613-634.

574 11. Carlton JG, Agromayor M, & Martin-Serrano J (2008) Differential requirements for Alix
575   and ESCRT-III in cytokinesis and HIV-1 release. *Proc Natl Acad Sci U S A*
576   105(30):10541-10546.

577 12. Lee HH, Elia N, Ghirlando R, Lippincott-Schwartz J, & Hurley JH (2008) Midbody
578   targeting of the ESCRT machinery by a noncanonical coiled coil in CEP55. *Science*
579   322(5901):576-580.

580 13. Mierzwa BE*, et al.* (2017) Dynamic subunit turnover in ESCRT-III assemblies is
581   regulated by Vps4 to mediate membrane remodelling during cytokinesis. *Nat. Cell
582   Biol.* 19(7):787-798.

14. Agromayor M & Martin-Serrano J (2013) Knowing when to cut and run: mechanisms that control cytokinetic abscission. *Trends Cell Biol* 23(9):433-441.

15. Norden C, *et al.* (2006) The NoCut pathway links completion of cytokinesis to spindle midzone function to prevent chromosome breakage. *Cell* 125(1):85-98.

16. Mendoza M, *et al.* (2009) A mechanism for chromosome segregation sensing by the NoCut checkpoint. *Nat Cell Biol* 11(4):477-483.

17. Steigemann P, *et al.* (2009) Aurora B-mediated abscission checkpoint protects against tetraploidization. *Cell* 136(3):473-484.

18. Mackay DR & Ullman KS (2015) ATR and a Chk1-Aurora B pathway coordinate postmitotic genome surveillance with cytokinetic abscission. *Mol Biol Cell* 26(12):2217-2226.

19. Nahse V, Christ L, Stenmark H, & Campsteijn C (2017) The Abscission Checkpoint: Making It to the Final Cut. *Trends Cell Biol* 27(1):1-11.

20. Carlton JG, Caballe A, Agromayor M, Kloc M, & Martin-Serrano J (2012) ESCRT-III governs the Aurora B-mediated abscission checkpoint through CHMP4C. *Science* 336(6078):220-225.

21. Capalbo L, *et al.* (2012) The chromosomal passenger complex controls the function of endosomal sorting complex required for transport-III Snf7 proteins during cytokinesis. *Open Biol* 2(5):120070.

22. Thoresen SB, *et al.* (2014) ANCHR mediates Aurora-B-dependent abscission checkpoint control through retention of VPS4. *Nat Cell Biol* 16(6):550-560.

23. Caballe A, *et al.* (2015) ULK3 regulates cytokinetic abscission by phosphorylating ESCRT-III proteins. *Elife* 4:e06547.

24. Pharoah PD, *et al.* (2013) GWAS meta-analysis and replication identifies three new susceptibility loci for ovarian cancer. *Nat Genet* 45(4):362-370, 370e361-362.

25. Bycroft C, *et al.* (2017) Genome-wide genetic data on ~500,000 UK Biobank participants. *bioRxiv*.

26. McCullough J, Fisher RD, Whitby FG, Sundquist WI, & Hill CP (2008) ALIX-CHMP4 interactions in the human ESCRT pathway. *Proceedings of the National Academy of Sciences of the United States of America* 105(22):7687-7691.

27. Ballesteros JA, Deupi X, Olivella M, Haaksma EE, & Pardo L (2000) Serine and threonine residues bend alpha-helices in the chi(1) = g(-) conformation. *Biophys. J.* 79(5):2754-2760.

28. Christ L, *et al.* (2016) ALIX and ESCRT-I/II function as parallel ESCRT-III recruiters in cytokinetic abscission. *J Cell Biol* 212(5):499-513.

29. Mackay DR, Makise M, & Ullman KS (2010) Defects in nuclear pore assembly lead to activation of an Aurora B-mediated abscission checkpoint. *J Cell Biol* 191(5):923-931.

30. Lafaurie-Janvore J, *et al.* (2013) ESCRT-III assembly and cytokinetic abscission are induced by tension release in the intercellular bridge. *Science* 339(6127):1625-1629.

31. Burrell RA, *et al.* (2013) Replication stress links structural and numerical cancer chromosomal instability. *Nature* 494(7438):492-496.

32. Olmos Y, Hodgson L, Mantell J, Verkade P, & Carlton JG (2015) ESCRT-III controls nuclear envelope reformation. *Nature* 522(7555):236-239.

33. Vietri M, *et al.* (2015) Spastin and ESCRT-III coordinate mitotic spindle disassembly and nuclear envelope sealing. *Nature* 522(7555):231-235.

34. Petsalaki E, Dandoulaki M, & Zachos G (2018) The ESCRT protein Chmp4c regulates mitotic spindle checkpoint signaling. *J. Cell Biol.*

35. Lukas C, *et al.* (2011) 53BP1 nuclear bodies form around DNA lesions generated by mitotic transmission of chromosomes under replication stress. *Nat. Cell Biol.* 13(3):243-253.

36. Amaral N, *et al.* (2016) The Aurora-B-dependent NoCut checkpoint prevents damage of anaphase bridges after DNA replication stress. *Nat Cell Biol* 18(5):516-526.

37. Janssen A, van der Burg M, Szuhai K, Kops GJ, & Medema RH (2011) Chromosome segregation errors as a cause of DNA damage and structural chromosome aberrations. *Science* 333(6051):1895-1898.

38. Santaguida S, Tighe A, D'Alise AM, Taylor SS, & Musacchio A (2010) Dissecting the role of MPS1 in chromosome biorientation and the spindle checkpoint through the small molecule inhibitor reversine. *J. Cell Biol.* 190(1):73-87.

39. Funk LC, Zasadil LM, & Weaver BA (2016) Living in CIN: Mitotic Infidelity and Its Consequences for Tumor Promotion and Suppression. *Dev Cell* 39(6):638-652.

40. Cancer Genome Atlas Research N (2011) Integrated genomic analyses of ovarian carcinoma. *Nature* 474(7353):609-615.

41. Toledo LI, *et al.* (2011) A cell-based screen identifies ATR inhibitors with synthetic lethal properties for cancer-associated mutations. *Nat Struct Mol Biol* 18(6):721-727.

42. Agarwal ML, Agarwal A, Taylor WR, & Stark GR (1995) p53 controls both the G2/M and the G1 cell cycle checkpoints and mediates reversible growth arrest in human fibroblasts. *Proceedings of the National Academy of Sciences of the United States of America* 92(18):8493-8497.

651 43. Capalbo L, *et al.* (2016) Coordinated regulation of the ESCRT-III component CHMP4C
652   by the chromosomal passenger complex and centralspindlin during cytokinesis. *Open*
653   *biology* 6(10).

654 44. Lata S, *et al.* (2009) Structure and function of ESCRT-III. *Biochem. Soc. Trans.* 37(Pt
655   1):156-160.

656 45. Tang S, *et al.* (2016) ESCRT-III activation by parallel action of ESCRT-I/II and
657   ESCRT-0/Bro1 during MVB biogenesis. *Elife* 5.

658 46. Tang S, *et al.* (2015) Structural basis for activation, assembly and membrane binding
659   of ESCRT-III Snf7 filaments. *Elife* 4.

660 47. Passerini V, *et al.* (2016) The presence of extra chromosomes leads to genomic
661   instability. *Nat Commun* 7:10754.

662 48. Santaguida S, *et al.* (2017) Chromosome Mis-segregation Generates Cell-Cycle-
663   Arrested Cells with Complex Karyotypes that Are Eliminated by the Immune System.
664   *Dev Cell* 41(6):638-651 e635.

665 49. Lezaja A & Altmeyer M (2017) Inherited DNA lesions determine G1 duration in the
666   next cell cycle. *Cell Cycle*:1-9.

667 50. Arora M, Moser J, Phadke H, Basha AA, & Spencer SL (2017) Endogenous
668   Replication Stress in Mother Cells Leads to Quiescence of Daughter Cells. *Cell Rep*
669   19(7):1351-1364.

670 51. Kalsbeek D & Golsteyn RM (2017) G2/M-Phase Checkpoint Adaptation and
671   Micronuclei Formation as Mechanisms That Contribute to Genomic Instability in
672   Human Cells. *Int J Mol Sci* 18(11).

673 52. Gatz SA & Wiesmuller L (2006) p53 in recombination and repair. *Cell Death Differ*
674   13(6):1003-1016.

675 53. Li K, *et al.* (2015) CHMP4C Disruption Sensitizes the Human Lung Cancer Cells to
676   Irradiation. *Int J Mol Sci* 17(1).

677 54. Cer RZ, Uma Mudunuri, R. Stephens, and Frank J. Lebeda. (2009) IC 50-to-K i: a
678   web-based tool for converting IC 50 to K i values for inhibitors of enzyme activity and
679   ligand binding. *Nucleic Acids Res.* 37(no. suppl_2):W441-W445.

680 55. Morita E, *et al.* (2011) ESCRT-III protein requirements for HIV-1 budding. *Cell host &*
681   *microbe* 9(3):235-242.

682 56. Olmos Y, Perdrix-Rosell A, & Carlton JG (2016) Membrane Binding by CHMP7
683   Coordinates ESCRT-III-Dependent Nuclear Envelope Reformation. *Curr. Biol.*
684   26(19):2635-2641.

685   57.   Fisher RD, *et al.* (2007) Structural and biochemical studies of ALIX/AIP1 and its role in
686   retrovirus budding. *Cell* 128(5):841-852.

687   58.   Soltis SM, *et al.* (2008) New paradigm for macromolecular crystallography
688   experiments at SSRL: automated crystal screening and remote data collection. *Acta
689   Crystallogr D Biol Crystallogr* 64(Pt 12):1210-1221.

690   59.   Gonzalez A, Tsai, Y. (2010) A Quick XDS Tutorial for SSRL
691   http://smb.slac.stanford.edu/facilities/software/xds/#autoxds_script.

692   60.   Kabsch W (2010) XDS. *Acta Crystallographica Section D: Biological Crystallography*
693   66(2):125-132.

694   61.   Kabsch W (2010) Integration, scaling, space-group assignment and post-refinement. .
695   *Acta Crystallographica Section D: Biological Crystallography* 66(2):133-144.

696   62.   Adams PD, Afonine, P.V., Bunkóczi, G., Chen, V.B., Davis, I.W., Echols, N., Headd,
697   J.J., Hung, L.W., Kapral, G.J., Grosse-Kunstleve, R.W. and McCoy, A.J., (2010)
698   PHENIX: a comprehensive Python-based system for macromolecular structure
699   solution. . *Acta Crystallographica Section D: Biological Crystallography* 66(2):213-221.

700   63.   McCoy AJ, Grosse-Kunstleve, R.W., Adams, P.D., Winn, M.D., Storoni, L.C. and
701   Read, R.J., (2007) Phaser crystallographic software. . *Journal of Applied
702   Crystallography* 40(4):658-674.

703   64.   Emsley P, Lohkamp, B., Scott, W.G. and Cowtan, K., (2010) Features and
704   development of Coot. . *Acta Crystallographica Section D: Biological Crystallography*
705   66(4):486-501.

706   65.   Afonine PV, Grosse-Kunstleve, R.W., Echols, N., Headd, J.J., Moriarty, N.W.,
707   Mustyakimov, M., Terwilliger, T.C., Urzhumtsev, A., Zwart, P.H. and Adams, P.D.,
708   (2012) Towards automated crystallographic structure refinement with phenix. refine. .
709   *Acta Crystallographica Section D: Biological Crystallography* 68(4):352-362.

710   66.   Chen VB, Arendall, W.B., Headd, J.J., Keedy, D.A., Immormino, R.M., Kapral, G.J.,
711   Murray, L.W., Richardson, J.S. and Richardson, D.C., (2010) MolProbity: all-atom
712   structure validation for macromolecular crystallography. . *Acta Crystallographica
713   Section D: Biological Crystallography* 66(1):12-21.

714   67.   Howlin B, S. A. Butler, D. S. Moss, G. W. Harris, and H. P. C. Driessen (1993)
715   "TLSANL: TLS parameter-analysis program for segmented anisotropic refinement of
716   macromolecular structures." *Journal of Applied Crystallography* 26,(no. 4):622-624.

717   68.   DeBoever C, *et al.* (2017) Medical relevance of protein-truncating variants across
718   337,208 individuals in the UK Biobank study. *bioRxiv*.

719 **Figures and Legends:**

Table 1. Significant association results for the rs35094336 genetic variant with multiple cancer types. 337,208 individuals from UKBiobank were analyzed. Results obtained from Global Biobank Engine, Stanford, CA (URL: http://gbe.stanford.edu/) [October, 2017]. The results show the association with the A (rs35094336) risk allele (CHMP4C^{T232}) compared to the G (CHMP4C^{A232}) reference allele.

Cancer Type	OR (95% CI)	P-value	Cases	Cancer code
Family Prostate*	1.04 (1.01 – 1.08)	0.007	34,359	FH1044
Male Genital Tract	1.12 (1.03 – 1.23)	0.012	3,449	1038
Skin	1.05 (1.01 – 1.09)	0.018	19,170	1003
Prostate	1.08 (1.01 – 1.16)	0.023	6,460	1044
Non-Melanoma Skin	1.05 (1.01 – 1.10)	0.024	16,791	1060
Ovarian	1.17 (1.01 – 1.36)	0.037	1,208	1039

*Association with family history of prostate cancer.
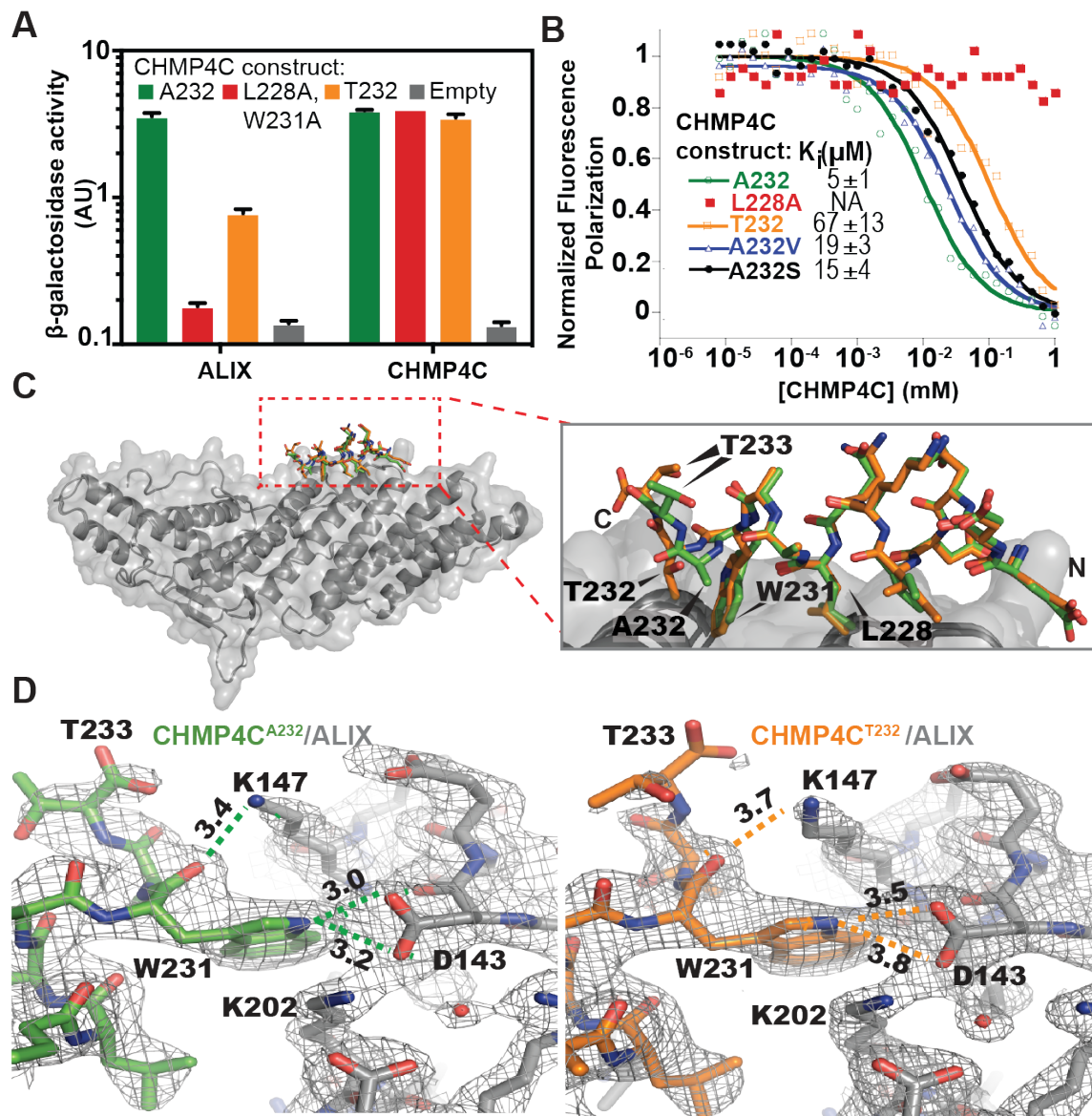OR (95% CI): Odds Ratio (95% Confidence Interval)

23

720

721
722
Figure. 1. The CHMP4C A232T substitution reduces ALIX binding.
723 **(A)** ß-galactosidase activity assays of yeast co-transformed with the indicated full-length
724 CHMP4C constructs fused to VP16 and full-length ALIX or CHMP4C fused to GAL4
725 (mean±SD, n=3). (**B**) Competitive fluorescence polarization binding assay with an ALIX
726 construct spanning the Bro1 and V domains (residues 1-698) binding to fluorescently labelled
727 CHMP4C[A232] peptide (residues 216-233) competed with the indicated unlabeled CHMP4C
728 peptides. Curves are from a representative experiment. K_i values are mean±SD. N≥7. (**C**)
729 (Left) Superposition of ALIX Bro1 domain (grey) complexes with CHMP4C[A232] (green) and
730 CHMP4C[T232] (orange) peptides. (Right) Expansion of the CHMP4C peptide superposition
731 highlights the reduction in CHMP4C[T232] helicity. (**D**) Binding interfaces between ALIX (grey)
732 and CHMP4C[A232] (left panel, green) and CHMP4C[T232] (right panel, orange). Figures show
733 equivalent intermolecular distances (Å) for different atoms of CHMP4C residue W231. See
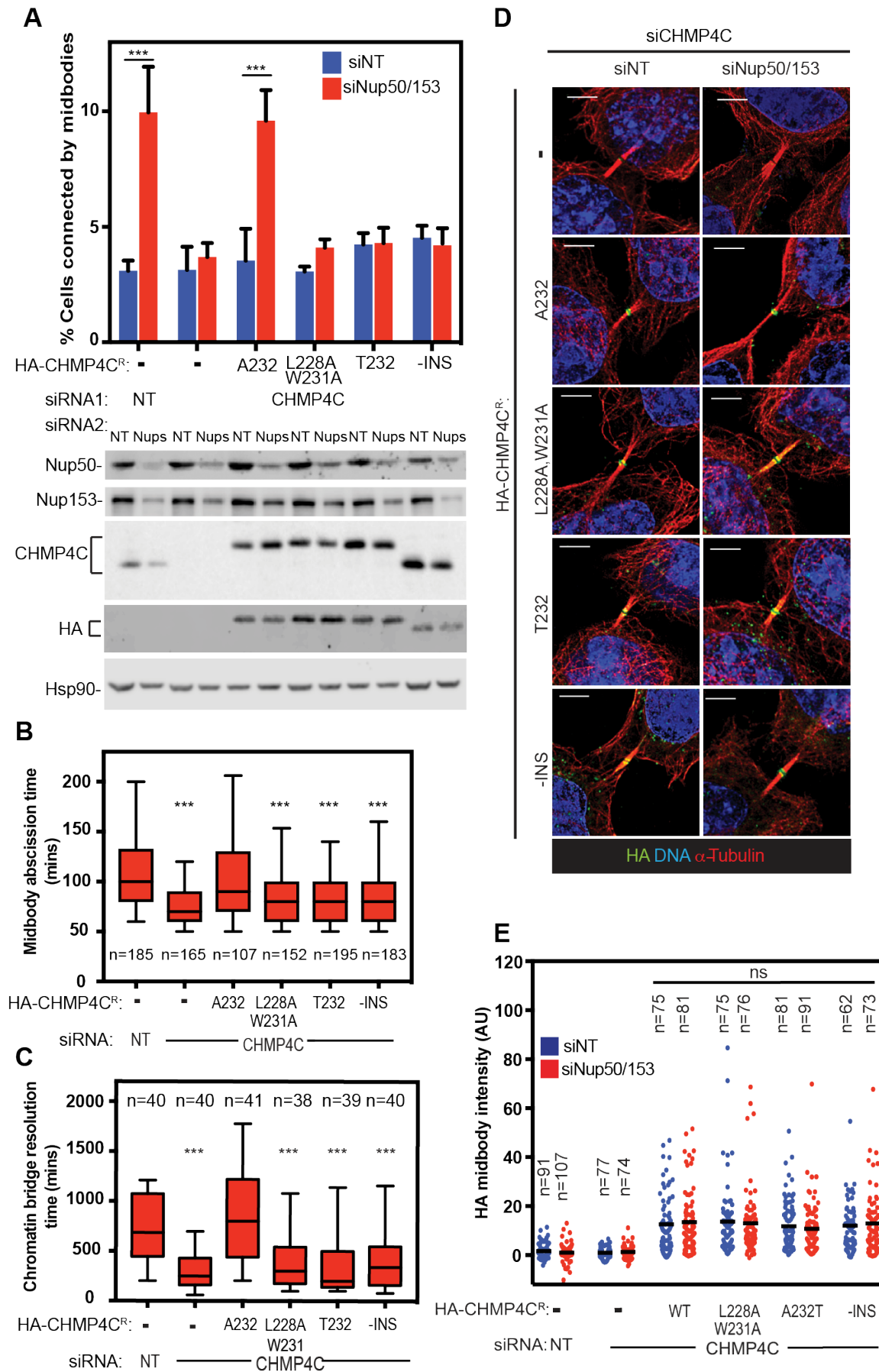734 also Fig. S1 and Table S1.
735

24

A

% Cells connected by midbodies

HA-CHMP4C^R: - - A232 L228A W231A T232 -INS
siRNA1: NT CHMP4C
siRNA2: NT Nups NT Nups NT Nups NT Nups NT Nups NT Nups

Nup50-
Nup153-
CHMP4C
HA
Hsp90-

siNT siNup50/153

B

Midbody abscission time (mins)

n=185 n=165 n=107 n=152 n=195 n=183

HA-CHMP4C^R: - - A232 L228A W231A T232 -INS
siRNA: NT CHMP4C

C

Chromatin bridge resolution time (mins)

n=40 n=40 n=41 n=38 n=39 n=40

HA-CHMP4C^R: - - A232 L228A W231 T232 -INS
siRNA: NT CHMP4C

D

siCHMP4C
siNT siNup50/153

HA-CHMP4C^R:
-
A232
L228A,W231A
T232
-INS

HA DNA α-Tubulin

E

HA midbody intensity (AU)

ns

n=75 n=81 n=75 n=76 n=81 n=91 n=62 n=73
n=91 n=107 n=77 n=74

siNT siNup50/153

HA-CHMP4C^R: - - WT L228A W231A A232T -INS
siRNA: NT CHMP4C

736

25

Figure 2. CHMP4C T232 does not support the abscission checkpoint.
(**A**) HeLa cells stably expressing siRNA resistant HA-CHMP4C constructs were treated with the indicated siRNA and stained for α-tubulin. (Top) percentage of midbody-arrested cells. Data are mean±SD from >3 separate experiments with n>900 cells. (Bottom) representative immunoblots from (A). (**B**) Asynchronous HeLa mCherry-Tubulin cells stably expressing siRNA resistant HA-CHMP4C constructs were transfected with the indicated siRNA and midbody abscission times were scored from ≥3 separate experiments. Here and throughout, box edges mark the 25th and 75th quartiles and whiskers mark 5-95% percentile. Bars denote the median. Mean times ±SD were non-targeting (NT): 110±47 min, siCHMP4C: 75±26 min HA-CHMP4C^{A232} + siCHMP4C, 108±47 min, HA-CHMP4C^{L228A,W231A} + siCHMP4C, 86±33 min, HA-CHMP4C^{T232} + siCHMP4C, 81±27 min, HA-CHMP4C^{-INS} + siCHMP4C, 87±44 min. See also Movies S1-S6. (**C**) HeLa cells stably expressing siRNA resistant HA-CHMP4C constructs and YFP-Lap2β were transfected with the indicated siRNA. Resolution time of Lap2β bridges were quantified from ≥3 separate experiments. Mean times ±SD were non-targeting (NT): 721±333 min, siCHMP4C: 296±187 min HA-CHMP4C^{A232} + siCHMP4C, 853±474 min, HA-CHMP4C^{L228A,W231A} + siCHMP4C, 415±317 min, HA-CHMP4C^{T232} + siCHMP4C, 396±394 min HA-CHMP4C^{-INS} + siCHMP4C, 421±341 min. See also Movies S7-S12. (**D, E**) HA-CHMP4C recruitment to midbodies determined by staining for DAPI (blue), α-tubulin (red) and HA (green) from ≥3 separate experiments. Scale bar, 5 μm. Data in (**E**) represent the staining intensity of HA normalized to background measurements. Mean value is marked. *P*-values were calculated using 2-way ANOVA and Sidak's multiple comparisons test, (**A**, **E**) or one-way ANOVA vs. control (HeLa siNT) (**B, C**), ***=p<0.001. Western blots for B, C, are shown in Fig. S2.
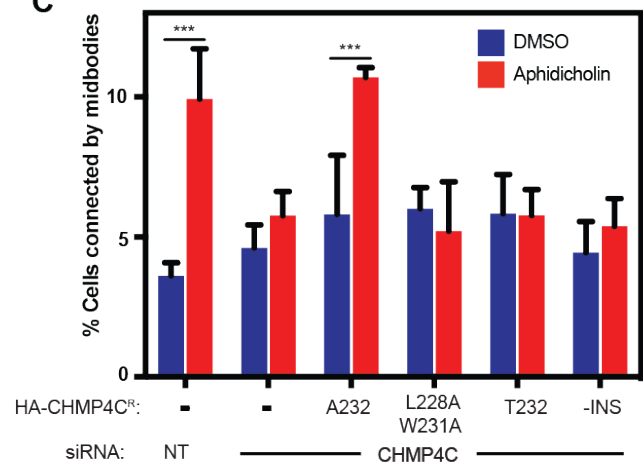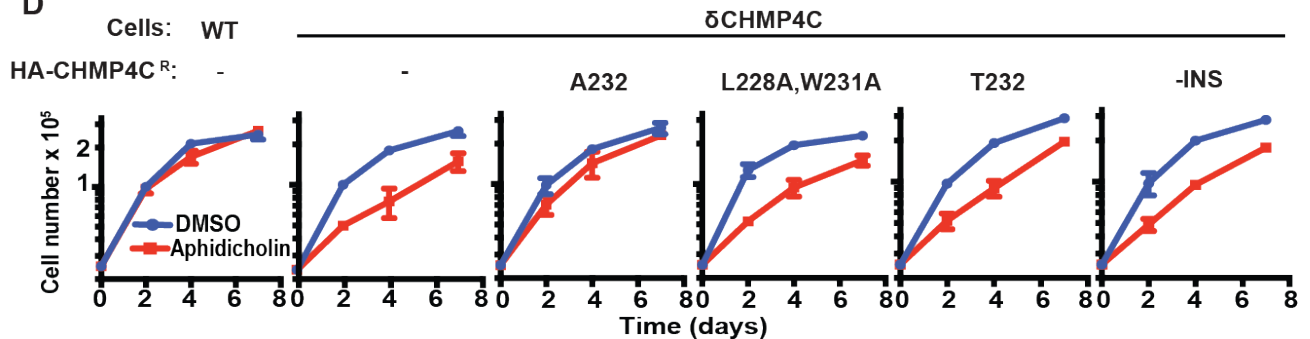
26
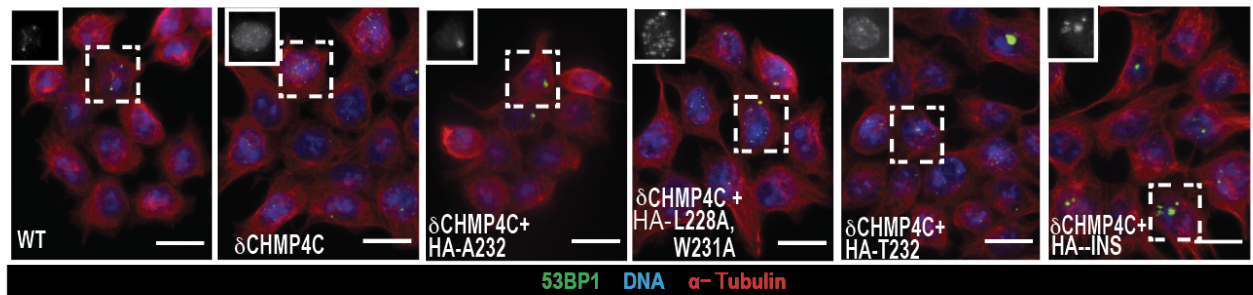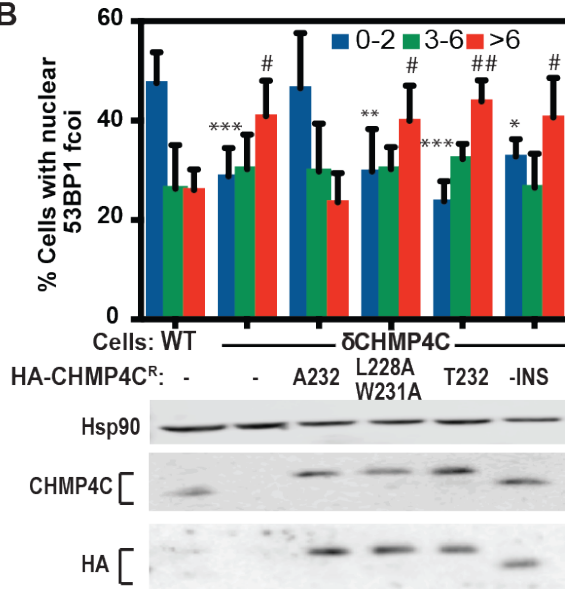
761
762 **Figure 3. Cells lacking the abscission checkpoint exhibit elevated genome damage**
763 **and are sensitized to replication stress.**
764 (**A**) HCT116 cells with (WT) or without endogenous CHMP4C (δCHMP4C) expressing the
765 indicated HA-CHMP4C construct were stained for 53BP1 (green), α-tubulin (red) and DAPI
766 (blue). Scale bars, 20 μm. Insets show grey scale images of boxed cells. (**B**) Numbers of
767 53BP1 foci/cell were determined from 3 independent experiments and binned into the
768 designated categories. Shown are mean±SD from >900 cells. *P*-value calculated using 2-way
769 ANOVA and Sidak's multiple comparisons test comparing each category to control (WT), *=
770 0-2 foci, #= >6 foci, */#$P < 0.05$ **/##=P<0.005, ***/###=P<0.001. (**C**) Cells stably expressing
771 the indicated HA-CHMP4C construct were treated with the indicated siRNA for 48 hours,
772 then with DMSO or 30 nM aphidicolin for 24 hours. The number of cells connected by
773 midbodies was scored. (**D**) HCT116^{WT} or HCT116^{δCHMP4C} cells expressing the indicated HA-
774 CHMP4C constructs were cultured in the continuous presence of DMSO (blue) or 30 nM
775 aphidicolin (red) and cell numbers were determined at the indicated time points. Plotted are
776 mean±SD from 3 independent experiments. See also Fig. S7*A*.
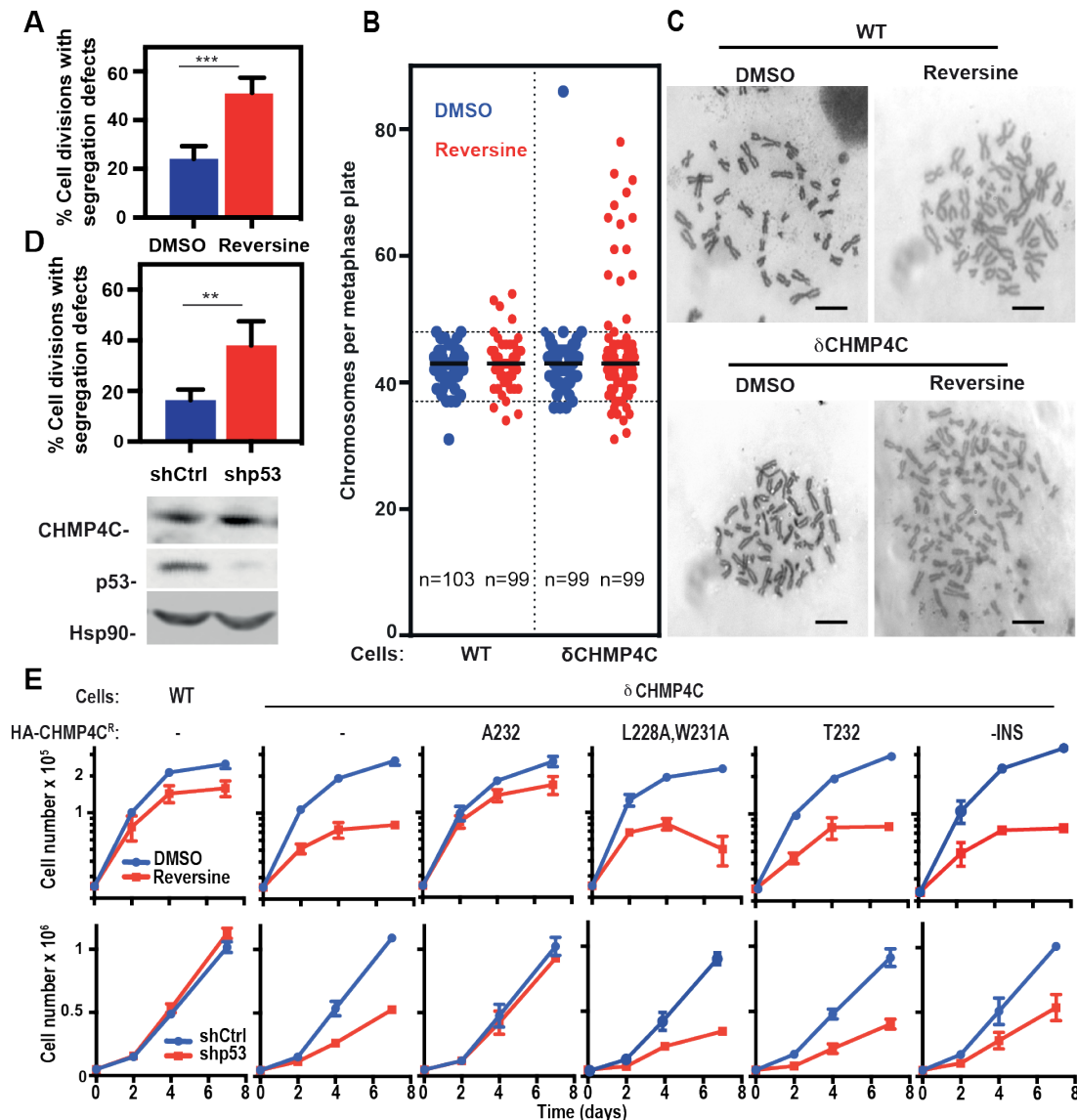
27

Figure. 4. Defects in chromosome segregation and the abscission checkpoint synergize to impair cell growth.

(**A**) HCT116 cells expressing histone H2B-mCherry were grown in the continuous presence of DMSO (blue) or 0.1 μM reversine (red) and anaphase segregation defects were scored. Data shown are mean±SD from n>130 cells from 3 separate experiments. See also Fig. S7*B*, *C*, and Movies S16-S19. (**B**) HCT116^{WT} or HCT116$^{\delta CHMP4C}$ were cultured for 48 hours in the continuous presence of DMSO (blue) or 0.1 μM reversine (red). Metaphases were enriched by overnight treatment with nocodazole, and chromosome number was determined. Plots show all data with medians marked. Extreme aneuploidy is defined as chromosome numbers above 48 or below 37 (dashed lines). Representative metaphase spreads can be seen in (**C**), scale bars, 10 μm. Data were collected from >4 independent experiments. (**D**) HCT116 cells expressing histone H2B-mCherry were depleted of p53 by shRNA treatment (shp53) and anaphase segregation defects were scored. Data are mean±SD, n>200, from 4 separate experiments across two shRNA transductions. See also Fig. S7*D*, S9*B*, *C*, and Movies S20-S23. (**E**) HCT116^{WT} or HCT116$^{\delta CHMP4C}$ cells expressing the indicated CHMP4C construct were (top panel) grown in the continuous presence of either DMSO (blue lines) or 0.1 μM reversine (red line) or (bottom panel) depleted of p53 by shRNA treatment (shCtrl, blue, shp53, red) and cell numbers were determined at the indicated time points. Data show are mean±SD from >3 independent experiments. *P*-values calculated using two-tailed unpaired Student's *t*-test, **P<0.005,***P<0.001. See also Fig. S9*A*.

28